Clinical Radiology xxx (xxxx) xxx

Contents lists available at ScienceDirect

Clinical Radiology

journal homepage: www.clinicalradiologyonline.net

Whole-body MRI: a practical guide for imaging patients with malignant bone disease

J.M. Winfield [a,b], M.D. Blackledge [a,b], N. Tunariu [a,b], D.-M. Koh [a,b], C. Messiou [a,b,*]

[a] *Division of Radiotherapy and Imaging, The Institute of Cancer Research, 123 Old Brompton Road, London, SW7 3RP, UK*

[b] *MRI Unit, Royal Marsden NHS Foundation Trust, Downs Road, Sutton, Surrey, SM2 5PT, UK*

ARTICLE INFORMATION

Article history:
Received 21 September 2020
Accepted 8 April 2021

Whole-body magnetic resonance imaging (MRI) is now a crucial tool for the assessment of the extent of systemic malignant bone disease and response to treatment, and forms part of national and international recommendations for imaging patients with myeloma or metastatic prostate cancer. Recent developments in scanners have enabled acquisition of good-quality whole-body MRI data within 45 minutes on modern MRI systems from all main manufacturers. This provides complimentary morphological and functional whole-body imaging; however, lack of prior experience and acquisition times required can act as a barrier to adoption in busy radiology departments. This article aims to tackle the former by reviewing the indications and providing guidance for technical delivery and clinical interpretation of whole-body MRI for patients with malignant bone disease.

Introduction

The assessment of the extent and response of systemic malignant bone disease to treatment represents a major unmet need in oncology. Skeletal metastases develop in up to two-thirds of cancer patients and the bone is the most common site for cancer spread in prostate (up to 90% of patients) and breast cancers (70% of patients).[1] Multiple myeloma, the most common primary bone marrow malignancy, has an incidence of over 5,000 cases per year and prevalence of about 17,600 people.[1]

Conventional imaging tests, e.g., computed tomography (CT) and radionuclide bone scintigraphy (BS), are widely used in the detection of malignant bone disease but lack sensitivity. Furthermore, the assessment of treatment response of bone disease is unreliable as most bone metastases are unevaluable by conventional CT criteria (e.g., response evaluation criteria in solid tumours, RECIST[2]) unless there is an associated soft-tissue component. The only recognised criteria for BS, the Prostate Cancer Working Group (PCWG), define progression/non-progression based on the development of two new lesions[3] that need to be confirmed by subsequent BS at 6–12 weeks. Whole-body

* Guarantor and correspondent: C. Messiou, MRI Unit, Royal Marsden Hospital, Downs Road, Sutton, Surrey, SM2 5PT, UK. Tel.: +44 20 8661 1378; fax: +44 20 8661 0846.
E-mail address: christina.messiou@rmh.nhs.uk (C. Messiou).

https://doi.org/10.1016/j.crad.2021.04.001

(WB) magnetic resonance imaging (MRI) has been reported to have similar or better diagnostic accuracy than integrated positron-emission tomography (PET)-CT for metastatic disease[4] and myeloma[5–7]; this holds particularly true for lesions that are PET tracer negative such as 2-[^{18}F]-fluoro-2-deoxy-D-glucose (FDG)-negative disease in lobular breast cancer or renal cell carcinoma and prostate-specific membrane antigen (PSMA)-negative disease in prostate cancer. WB-MRI is non-invasive, well tolerated by patients, is low-risk unless MRI is contraindicated, and facilitates long-term monitoring without radiation burden; the latter point is influential in directing patient preference for WB-MRI.[5,8] In addition, MRI is highly accurate for assessing skeletal complications such as metastatic spinal cord compression (MSCC) and vertebral fractures.

In prostate cancer, next-generation WB-MRI (including diffusion-weighted [DW] MRI and Dixon imaging) is useful for assessing the response of metastatic bone disease,[9,10] and is recommended in the latest American Society of Clinical Oncology (ASCO) guidelines for advanced prostate cancer in staging and detection of progression.[11] Specifically, the guideline suggests WB-MRI when conventional imaging is suspicious/equivocal or when detection of additional sites will alter management; and for therapy monitoring where there is high suspicion for progression despite stable conventional imaging; however, it is important to recognise that when minor disease progression on WB-MRI is used to trigger a change in therapy, there is potential for lead-time bias with apparent improvements in survival, which should be considered when interpreting the results.[12]

The International Myeloma Working Group (IMWG) now recognises the presence of more than one focal bone marrow lesion >5 mm on MRI as an indication for starting systemic treatment for patients with suspected myeloma.[13] In 2016, National Institute for Health and Care Excellence (NICE) guidelines positioned WB-MRI as the imaging technique of choice for all patients with a suspected diagnosis of myeloma in the UK with increasing evidence and adoption for monitoring, response assessments, and restaging.[14] The guidance from NICE was based not only on diagnostic accuracy but compelling quality of life and health economics analyses.[15] The increased sensitivity of WB-MRI in detecting focal myeloma lesions in the bone marrow allows accurate distinction between patients with multiple myeloma who require and will derive survival benefit from treatment from those with high-risk asymptomatic myeloma who would not benefit from treatment.[13] As WB-MRI is non-invasive, it is also attractive as a surveillance tool for higher risk asymptomatic patients for early detection of progression.

The high soft-tissue contrast, good spatial resolution, wide anatomical coverage and non-invasive nature of WB-MRI can potentially lead to disruption of existing clinical pathways for managing systemic malignant bone disease, by providing faster and more accurate assessment of disease and response to treatment, which can lead clinicians towards more confident and cost-effective decision-making, leading to improved outcomes. The evidence for the use of WB-MRI combined with NICE guidance for patients with myeloma has created huge demand for training, which in part is being addressed by interactive training courses, which have been ongoing over the past few years[16] in addition to international consensus documents to support acquisition and reporting.[17,18] We are of course mindful that lack of capacity also presents a significant barrier to adoption.[19] Compared with data from the Organisation of Economic Cooperation and Development (OECD), the UK has one of the lowest number of MRI systems per capita.[20] It is hoped that in part this will be addressed by the UK government's commitment of £200 million for cancer screening, which will include investment in new scanners.

At Royal Marsden NHS Foundation Trust, we have been providing a WB-MRI service for 9 years, delivering more than 5,300 scans over that time. In this article, we aim to share the experience gained, providing insights into WB-MRI protocol composition, and how that can be optimally translated into an invaluable suite of evidence for directing patient care.

WB-MRI protocols

WB imaging may extend from the eyes to the mid thighs (metastatic bone disease) or skull vertex to knees (myeloma), depending on the clinical application, local preferences, and the ability of the patient to tolerate the examination. Images are acquired in stations, with usually five to seven stations to cover the WB, depending on the scanner and required coverage. The couch is moved through the scanner between stations, in order to position the imaging volume at the isocentre of the magnet for acquisition of each station. WB receiver coil coverage is required. Modern MRI scanners can provide WB coverage using multiple receiver coils, without the need to reposition coils or the patient during the examination. The integral body coil is not conventionally used to receive the MR signal in WB-MRI examinations.[21] WB table movement is required in order to move each imaging station to the isocentre of the magnet and is therefore an increasingly important specification for procurement of new scanners. Sufficient distance is required between the magnet and the walls of the scanner room in order to allow WB table movement, which should be considered when designing a new MRI facility.

Images are usually acquired axially, and it is desirable to match slice positions between imaging sequences to facilitate direct comparison. Composed series are constructed by combining images acquired at separate stations to form a new series for each imaging contrast. Most modern MRI systems are able to produce composed series on the console using automated processing steps during the WB-MRI examination. Some older models may require composed series to be produced by the operator as a post-processing step on the scanner console or on a separate workstation.

Recommendations have been published for the imaging protocols, interpretation, and reporting of whole-body MRI in some of the more common applications: Myeloma

Please cite this article as: Winfield JM et al., Whole-body MRI: a practical guide for imaging patients with malignant bone disease, Clinical Radiology, https://doi.org/10.1016/j.crad.2021.04.001

Response Assessment and Diagnosis System (MY-RADS) in myeloma[17] and METastasis Reporting and Data System for Prostate Cancer (MET-RADS-P) in advanced prostate cancer.[18] MY-RADS and MET-RADS-P both recommend core protocols for disease detection (approximately 45 minutes scan time) and comprehensive protocols (up to 1 hour scan time) for assessment of soft tissues or for use in clinical trials. The core and comprehensive protocols are described in Table 1 and an example core acquisition of MY-RADS is shown in Fig 1. The core protocols consist of sagittal spine imaging, axial WB-DW-MRI with two b-values (low b-value 50–100 s/mm^2 and high b-value 800–900 s/mm^2 [MY-RADS] or 800–1,000 s/mm^2 [MET-RADS-P]), axial or coronal T1T1-weighted (W) Dixon, and optional axial T2W single-shot fast/turbo spin echo (ss-FSE/TSE) imaging. The comprehensive protocols include the same sequences as the core protocols but are extended by the addition of an intermediate b-value (500–600 s/mm^2) in the DW-MRI to facilitate quantitative measures of response, additional coronal T1W Dixon imaging, which can help visualise extent of disease in long bones, T2W ss-FSE/TSE imaging, which supports anatomical correlation and assessment of soft tissues, and selected regional assessments. The imaging sequences and coverage recommended in the MY-RADS and MET-RADS-P protocols can be achieved using modern MRI systems from all of the main manufacturers.

Image acquisition and clinical application of WB-MRI

Sagittal imaging of the spine

Technical background

Sagittal spine imaging is usually acquired using fast/turbo spin echo (FSE/TSE) sequences, which provide high-resolution images (approximately 1.0 mm × .01 mm in-plane voxel dimensions) with minimal geometric distortion in acceptable acquisition times.[22] Guidelines for WB-MRI recommend acquisition of T1W images plus either short-tau inversion recovery (STIR),[23] T2W, or fat-

Table 1
Summary of imaging protocols described in MY-RADS[16] and MET-RADS-P[17] recommendations.

Image/contrast	MY-RADS[16]		MET-RADS-P[17]	
	Core protocol	Comprehensive protocol	Core protocol	Comprehensive protocol
Diffusion-weighted imaging	Whole body (vertex to knees[a]); axial; diffusion-weighted; STIR fat suppression; 5 mm[a] contiguous slices; multiple stations; two b-values (50–100 and 800–900 s/mm^2 [a]); ADC estimated using mono-exponential fitting; MIP of highest b-value images	As described in core protocol, with additional b-value (500–600 s/mm^2)	Whole body (skull base to mid-thighs[a]); axial; diffusion-weighted; STIR fat suppression; 5–7 mm[a] contiguous slices; multiple stations; two b-values (50–100 s/mm^2 and 800–1,000 s/mm^2 [a]); ADC estimated using mono-exponential fitting; coronal reformat[a] and MIP of highest b-value images	As described in core protocol, with additional b-value (500–600 s/mm^2)
T1W Dixon imaging	Whole body (vertex to knees[a]); axial or coronal; T1W gradient echo Dixon; 5 mm section thickness; fat and water image reconstructions; estimate fat fraction maps[a]. (3D T1W FSE/TSE may be performed as alternative)	As described in core protocol, with axial and coronal imaging	Whole body (vertex to mid-thighs[a]); axial (5 mm sections) or coronal (2 mm[a]); T1W gradient echo Dixon; fat images must be reconstructed. (3D T1W FSE/TSE may be performed as alternative)	As described in core protocol, with axial and coronal imaging
T2W imaging	Whole body (vertex to knees[a]); axial; FSE/TSE; no fat suppression; 5 mm contiguous slices; multiple stations; preferably matching diffusion-weighted images; optional in core protocol	As described in core protocol; should always be performed in comprehensive protocol	Whole body (vertex to mid-thighs[a]); axial; FSE/TSE; no fat suppression; 5 mm contiguous slices; multiple stations; preferably matching diffusion-weighted images; optional in core protocol	As described in core protocol; should always be performed in comprehensive protocol
Spine	Sagittal whole spine; 4–5 mm slice thickness. T1W FSE/TSE and STIR or T2W fat-suppressed imaging	As described in core protocol	Sagittal whole spine; 4–5 mm slice thickness. T1W fast FSE/TSE and STIR or T2W fat-suppressed imaging	As described in core protocol
Regional assessments	Not usually acquired	Optional	None	Dedicated prostate, small field-of-view spine, brain, and contrast enhancement

Both recommendations include core protocols and comprehensive protocols.
STIR, short tau inversion recovery; ADC, apparent diffusion coefficient; MIP, maximum intensity projection; FSE/TSE, fast spin echo/turbo spin echo; T1W, T1-weighted; T2W, T2-weighted.
[a] The small differences between MY-RADS and MET-RADS-P recommendations.

Please cite this article as: Winfield JM et al., Whole-body MRI: a practical guide for imaging patients with malignant bone disease, Clinical Radiology, https://doi.org/10.1016/j.crad.2021.04.001

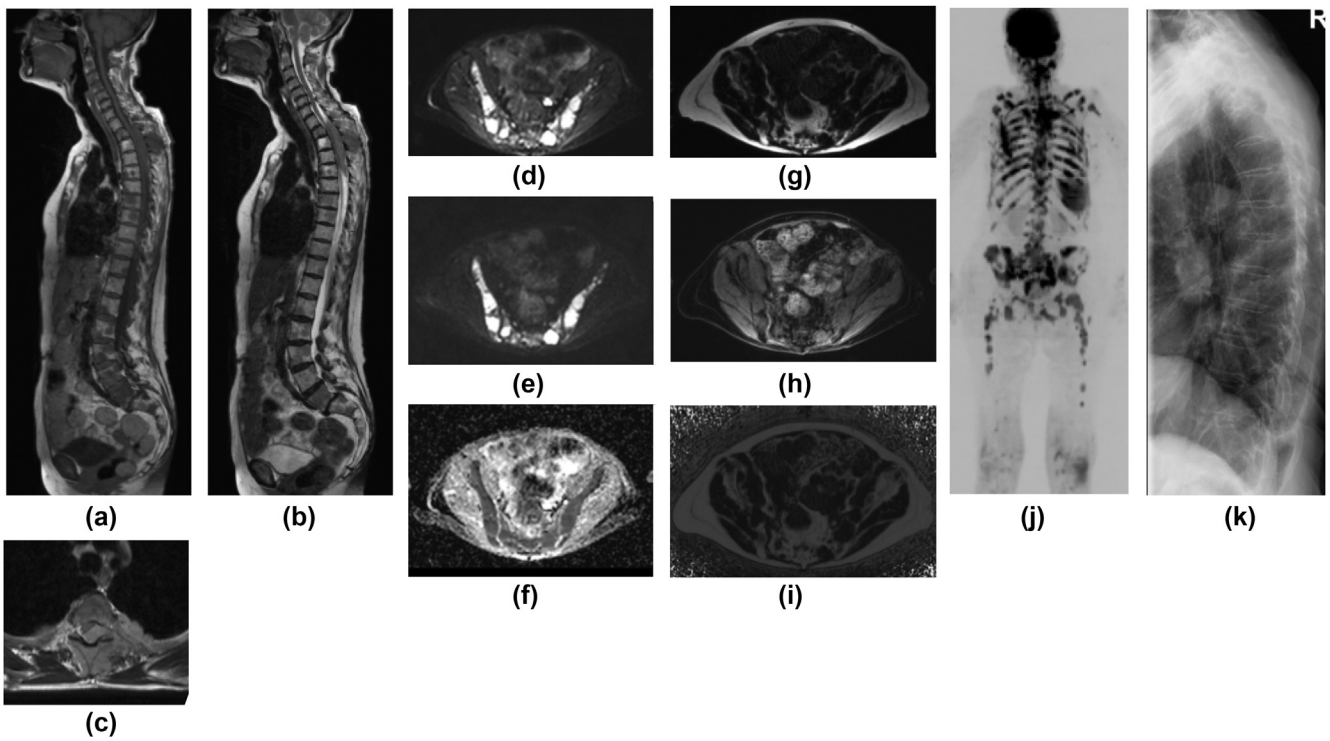

Figure 1 Core MY-RADS protocol in a patient with multifocal myeloma bone disease. (a) Sagittal T1W and (b) T2W images. (c) Supplemental axial T2W images; (d) axial b = 50 s/mm^2 DW-MRI; (e) b = 900 s/mm^2 and (f) ADC map from DW-MRI acquisition. (g) Axial fat-only (h) water-only and (i) FF map from Dixon MRI. (j) Inverted grey-scale b = 900 s/mm^2 MIP. Despite the large burden of multifocal disease and cord compression in (a-c), the skeletal survey was reported as negative for focal bone disease (k, lateral thoracic spine radiography).

suppressed T2W images, with axial series added if required.[17,18] Some centres may choose to use modified versions of their standard whole-spine protocol in order to reduce acquisition times, for example by reducing the number of signal averages, if acceptable image quality can be achieved. At Royal Marsden NHS Foundation Trust, we chose to omit the anterior saturation band to enable sagittal views of the sternum, which may be involved by disease.

Clinical applications

Sagittal imaging of the spine constitutes a crucial component of the WB-MRI protocol providing the ability to assess for disease, which may be threatening the spinal canal and/or nerve roots (Fig 1). Such findings are the most common indication for urgent contact with the clinical team following WB-MRI, although acute fractures, particularly those causing canal stenosis, should also be flagged urgently. Morphological features of convex vertebral body posterior margins, soft-tissue components, and involvement of pedicles can help to diagnose malignant rather than benign vertebral fractures and use of a localiser facilitates labelling the level of vertebral abnormalities identified on axial imaging. Although morphological detail from sagittal MRI sequences are often the cornerstone of characterising vertebral fractures, supplementary information from DW-MRI also contributes to aging and differentiating benign from malignant fractures as malignant marrow tends to exhibit impeded diffusion.[24]

WB-DW-MRI

Technical background

Diffusion is the motion of molecules due to their thermal energy.[25] Diffusion of water molecules in tissues can be impeded by boundaries, such as cell membranes.[26] Many tumour types exhibit impeded diffusion compared with normal tissues, thus providing a valuable contrast mechanism in oncology.[27]

WB-DW-MRI is usually acquired using single-shot echo-planar imaging (EPI) in clinical applications.[28,29] Magnetic field gradients are applied either side of the 180° refocusing pulses to sensitise the image contrast to the motion of water molecules.[30] The net effect of the diffusion gradients is to reduce the signal from tissues where the motion of water molecules is less impeded, whereas the signal is retained in tissues where the motion of water molecules is more impeded. Regions where diffusion is more impeded thus appear bright on DW images, against a background of low signal from less impeded regions.

The degree of diffusion weighting is often described using a “b-value”(units s/mm^2), which depends on the

strength of the diffusion gradients and their timings. A higher b-value corresponds to a more heavily diffusion weighted image. Two or three diffusion-weightings (b-values) are usually acquired. Larger numbers of b-values would lead to unreasonably long acquisition times for WB-DW-MRI. A low b-value of 50–100 s/mm^2 is usually used, rather than 0 s/mm^2, to reduce the influence of perfusion on apparent diffusion coefficient (ADC) estimates.[31]

The degree of impeded diffusion can be quantified using the ADC(units mm^2/s), which is estimated by fitting a mono-exponential decay function to the signal acquired at two or more b-values.[30] ADC maps should be viewed alongside diffusion-weighted images. The manufacturer's software should be capable of producing ADC maps (using mono-exponential fitting of the b-value signal intensity data) as an automated processing step carried out on the scanner console as part of the DW-MRI acquisition.

Contiguous slices should be acquired. The size of each imaging station in the head–foot direction should not exceed approximately 20 cm depending on the scanner.[32] It is undesirable to use larger imaging stations, even if the imaging sequence permits a larger number of slices, due to magnetic field inhomogeneity at the edges of a very large field-of-view (FOV) and non-linearities in the magnetic field gradients at larger distances from the isocentre of the magnet. Gradient non-linearities lead to spatial variation in the diffusion weighting, which causes bias in ADC estimates and thus impairs quantitative analysis.[32,33] A slice thickness of 5 mm is usually used,[34–36] although thicker slices may be used where rapid acquisitions are required, for example in some screening protocols.[37] The in-plane dimensions of the acquired voxels are usually between 2.5 mm × 2.5 mm and 3.5 mm × 3.5 mm,[35,36] although interpolation is often used to reconstruct images with smaller in-plane voxel dimensions. Acquisition of substantially smaller voxels would result in unacceptably low signal-to-noise ratio (SNR), particularly at high b-values, which impedes qualitative interpretation and may introduce systematic errors (bias) in ADC estimates.[38]

EPI is strongly affected by geometric distortion artefacts, arising from magnetic field inhomogeneities, for example, near metal hips or air in the stomach, and at the edges of a large FOV.

Good fat suppression across the whole FOV is essential for WB-DW EPI. Unsuppressed fat signal appears very bright in DW-MRI due to the low ADC of fat and, furthermore, exhibits a large chemical shift in the phase encoding direction.[39] Unsuppressed fat may therefore obscure features of interest, and degrades maximum intensity projections (MIPs), which are often used to view composed high-b-value images. STIR is used to achieve good fat suppression throughout the WB. STIR provides robust fat suppression in regions of relatively poor B_0 homogeneity, whereas spectral fat suppression methods often fail in these areas, for example, near the neck and shoulders and at the edges of the FOV.[40,41]

Clinical applications

DW-MRI is the most sensitive sequence for identification of bone marrow lesions[42] and is recognised as a biomarker of response.[43] For patients with metastatic bone disease, accurate delineation can guide selection of patients with oligometastatic disease for targeted treatment, or aid assessment of response/progression to therapy when CT and BS appearances are static (Fig 2) or confounded by possible osteoblastic flare that requires additional imaging. A randomised controlled trial has shown overall survival benefit for patients with oligometastatic disease treated with stereotactic ablative radiotherapy versus standard of care.[44] In patients with myeloma, the presence of more than one focal lesion with diameter ≥5 mm is crucial for establishing need for systemic treatment whereas large solitary plasmacytomas may be treated with radiotherapy alone.[13] Assessing distribution of disease for patients with myeloma must also include a specific assessment of the bone marrow trephine sites (posterior iliac crests) as this presents an opportunity to judge potential for sampling error, which arises from blind sampling. Although focal lesions are often identified on b = 900 s/mm^2 images, correlation with all other sequences is mandatory to avoid false-positive findings due, for example, to "T2 shine-through" which may occur from treated lesions, haemangiomas, infection, bone infarction, fractures, and artefacts around metal implants[14] (Fig 3). Similarly, although the b = 900 s/mm^2 MIP serves as a useful overview of disease burden, it should never be viewed in isolation as T2 shine-through effects cannot be distinguished and small volume disease is poorly resolved (Fig 4). The MIP images are, however, helpful for identification of rib or spinous process lesions, which are easily overlooked on axial series. False-negative reports after review of DW-MRI can occur when background diffuse hypercellularity obscures focal lesions. Therefore, the Dixon imaging should always be carefully interrogated for focal lesions where marrow appears diffusely hypercellular.

Arguably the most important contribution of DW-MRI is the capability to assess response/progression independent of changes in lesion size through measurement of ADC, in combination with DW-MRI signal intensity and T1W Dixon morphological images, which has led to response criteria such as MET-RADS-P and MY-RADS[17,18,35,45,46] (Fig 4). Reduced cellularity in treated focal bone marrow lesions results in increasing ADC values. Both ADC and disease volume are relevant depending on the clinical scenario. When looking at progression, the volume of disease matters more than minor changes in ADC. When looking at response, the significant increase in ADC matters more than volume as bone disease may not change its size/volume at the onset of disease response. In cases where normal marrow fat is restored, for example, diffuse disease responding to treatment, it is possible for ADC to fall and the returning marrow can be confirmed on Dixon MRI; however, it should be noted that although there is early

Please cite this article as: Winfield JM et al., Whole-body MRI: a practical guide for imaging patients with malignant bone disease, Clinical Radiology, https://doi.org/10.1016/j.crad.2021.04.001

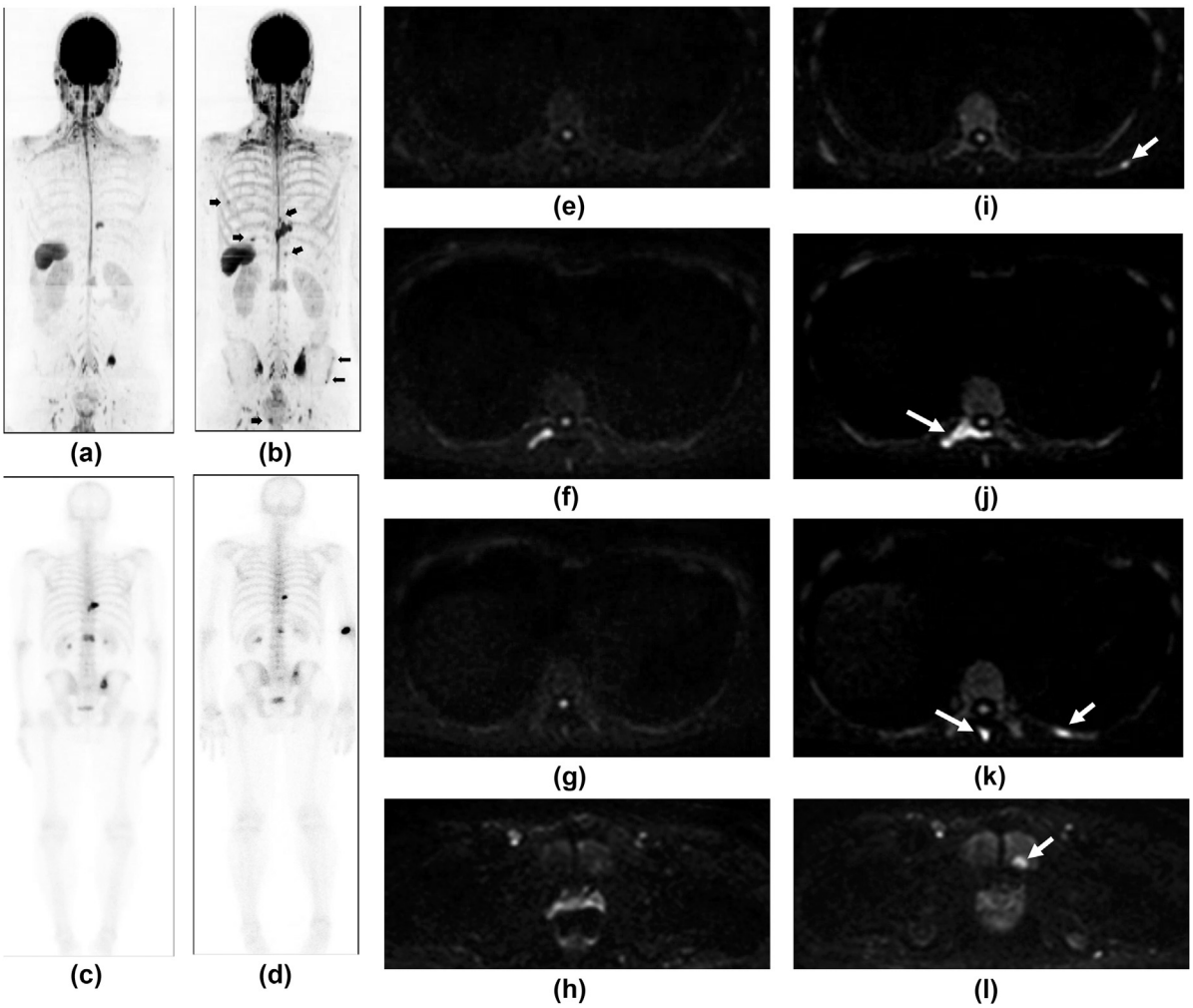

Figure 2 WB-MRI demonstrates progressive metastatic bone disease whilst BS remains stable in a 66-year-old man with bone-only metastatic prostate cancer at baseline and after therapy. (a) Posterior view b = 900 s/mm^2 MIP at baseline and (b) after 3 months follow-up. (c) BS before and (d) after 3 months follow-up and (e–h) representative axial b = 900 s/mm^2 DW-MRI before and (i–l) after 3 months follow-up. BS shows now new lesions and therefore no progression by radiological PCWG criteria. PSA rise (19–60 μg/l). MRI shows multiple new bone lesions and significant increase in size of the pre-existent lesions (arrows).

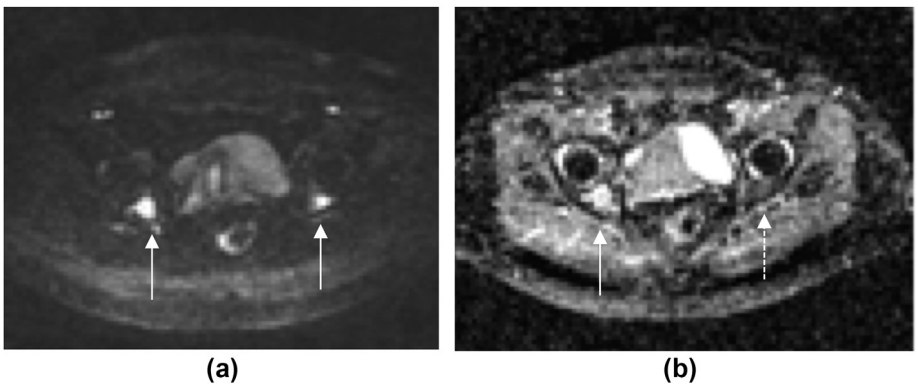

Figure 3 T2 shine-through. (a) Axial b = 900 s/mm^2 DW-MRI of a patient with suspected relapsed myeloma shows bilateral acetabular lesions (arrows); (b) however, the corresponding ADC map shows that the lesion on the right returns a high ADC equivalent to fluid in the bladder confirming this to be an acellular treated lesion (arrow). The high signal on the b = 900 s/mm^2 image represents T2 shine-through. Conversely, the lesion in the left acetabulum shows impeded diffusion in keeping with an active focal lesion (dashed arrow).

Please cite this article as: Winfield JM et al., Whole-body MRI: a practical guide for imaging patients with malignant bone disease, Clinical Radiology, https://doi.org/10.1016/j.crad.2021.04.001

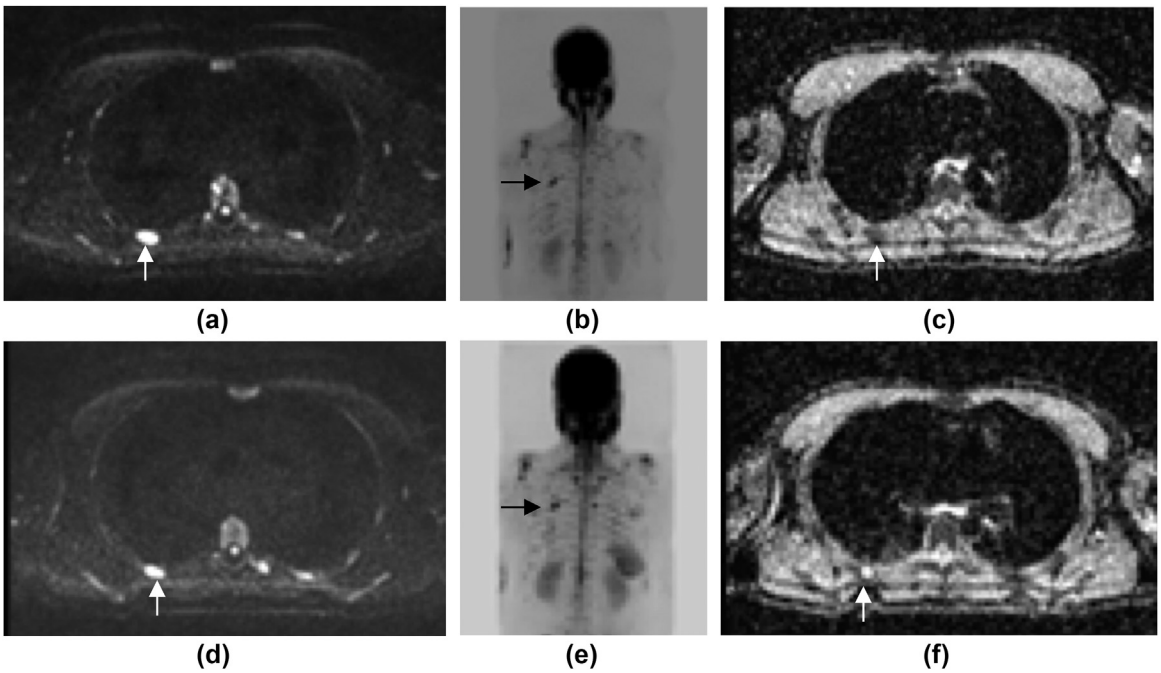

Figure 4 (a–c) Axial b = 900 s/mm^2 DW-MRI, b = 900 s/mm^2 MIP, and ADC map pre- and (d–f) post-chemotherapy in a patient with myeloma. The right posterior rib lesion (arrows) appears unchanged following treatment on b = 900 s/mm^2 and MIP images; however, the ADC map confirms that the lesion showed impeded diffusion at baseline and high ADC following treatment in keeping with response. Post-treatment signal on b = 900 s/mm^2 images represents T2 shine-through.

evidence that WB-MRI imaging responses may relate to clinical benefit, using WB-MRI to assess bone disease response or treatment benefit has not yet translated into clinical guidelines. Diffuse involvement can be suspected from diffuse decreased signal on T1W FSE/TSE or Dixon in-phase and fat-only images, and diffuse increased signal throughout the marrow relative to normal muscle on high b-value images; however, there is potential for false-positive appearances due to young age, rebound hypercellularity related to treatment effects, or granulocyte colony stimulating factor.[17,47] For patients with myeloma, the diagnosis of diffuse disease must be confirmed with trephining, as diffuse MRI changes are not specific and not included in the diagnostic IMWG criteria.[13] The ADC map also allows differentiation of active/cellular sites from treated/acellular sites at restaging (Fig 3). There is work in progress towards delivery of software tools that could allow whole-tumour burden assessment in diffuse disease and assessment of multiple lesions. Currently, the radiologist will choose representative lesions or areas for targeted quantitative evaluation. DW-MRI also allows detection and response assessments of extramedullary disease in myeloma patients[48] and nodal, visceral (e.g., liver, peritoneum) and intra-muscular metastases in non-myeloma patients, which are areas where MRI is recognised to have increased sensitivity compared with CT (Fig 5); this can be achieved using a combination of RECIST and DW-MRI criteria. In addition, review of both low and high b-value DW-MRI can detect CT-occult pathological fractures and avascular necrosis.[49]

Fat/water (Dixon) imaging

Technical background

Dixon imaging exploits the difference in resonance frequency between hydrogen nuclei attached to fat and water molecules in order to reconstruct images showing only fat and only water-based tissues.[50] Implementations differ between manufacturers, with differences in the number of echoes, spectral model of fat, and processing methods being employed.[51]

Fat and water images highlight regions where the fat content differs from surrounding tissues. Some implementations of Dixon imaging also produce fat fraction (FF) maps. Alternatively, fat and water images can be used to produce estimates of FF, often using calculation tools available on the scanner console or workstation ($FF = 100 \times S_F/(S_F + S_W)$), where S_F and S_W are the pixel values in the fat-only and water-only images respectively, and FF is expressed as a percentage; some centres/manufacturers prefer to use a factor of 1,000, rather than 100, which may aid windowing the FF maps).

Dixon images are usually acquired using three-dimensional (3D) gradient-echo sequences, with acceleration techniques to reduce acquisition times to <20 seconds per imaging station. Breath-hold acquisitions may be used in abdominal and thoracic stations.

Centres may choose to acquire T1W Dixon imaging or proton density weighted (PDW) Dixon imaging. T1W Dixon imaging has the advantage of providing T1W images alongside fat and water images, thus removing the

Please cite this article as: Winfield JM et al., Whole-body MRI: a practical guide for imaging patients with malignant bone disease, Clinical Radiology, https://doi.org/10.1016/j.crad.2021.04.001

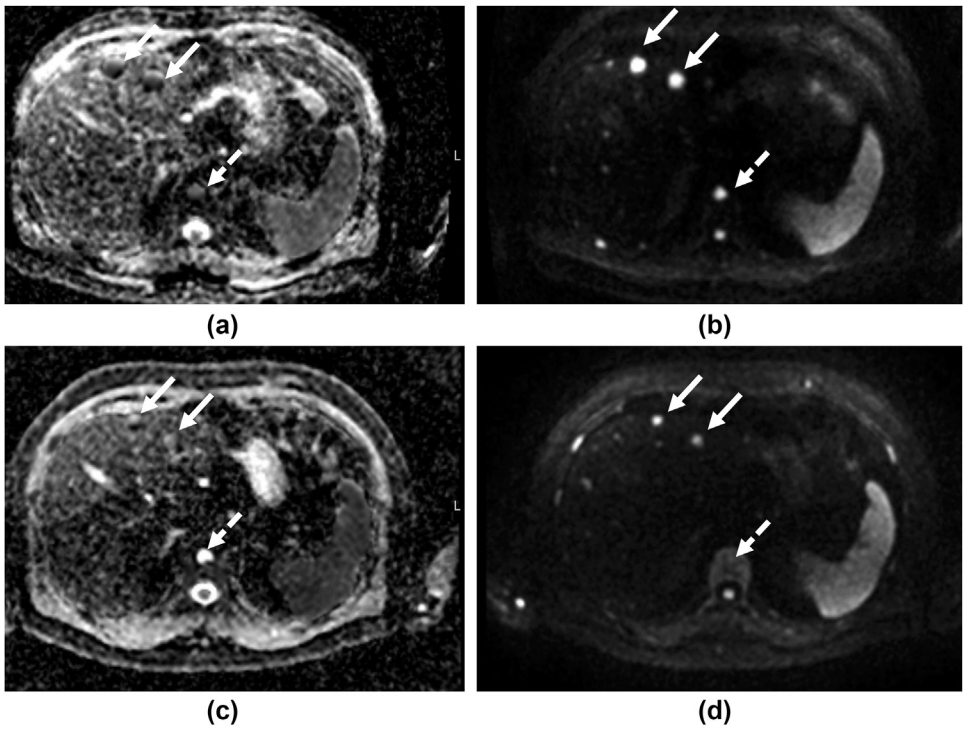

Figure 5 Hepatic and bone disease responding to 6 cycles of docetaxol treatment in a patient with advanced prostate cancer. (a,b) Axial ADC map and b = 900 s/mm^2 DW-MRI before and (c,d) after 6 cycles of treatment demonstrates sites of disease in the liver (white arrows) and T11 (white dashed arrows). Following treatment, there is a decrease in size of the liver lesions and increase in ADC of the liver and bone lesions.

requirement for additional T1W sequences; however, FF estimates from T1W Dixon images are less accurate that those from PDW images.[52–54] T2W TSE Dixon imaging is also available on many modern MRI systems[55] and has been demonstrated for bone marrow imaging,[56,57] but is not yet widely used in WB-MRI.

Fat/water swaps may occur in Dixon imaging, but occur less often in more recent Dixon algorithms. Fat/water swaps may be global, where the whole image is incorrectly labelled as fat or water, or local, where parts of the image show fat and parts show water-based tissues. Fat/water swaps are detrimental to FF estimates, although global fat/water swaps can be re-assigned by the user. Fat/water swaps are more likely to occur in regions of B_0 inhomogeneity, such as near metal implants, skin folds, or at locations far from the isocentre of the magnet. The likelihood of fat/water swaps can be reduced by removing metal objects where possible, positioning the patient centrally on the couch, and limiting the size of the FOV.

Clinical applications

The early clinical application for Dixon MRI was primarily to provide anatomical correlation for findings on DW-MRI (Fig 6); however, Dixon is also extremely helpful in patients with a background of diffuse marrow hypercellularity or rib lesions where the contrast between focal lesion and background marrow cannot be distinguished on DW-MRI. In such circumstances, it is important to interrogate the Dixon MRI images where the contrast can be better maintained through a different mechanism (Fig 7); however, Dixon is also a quantitative technique and measures of fat and water in bone marrow are also used to reflect response.[45,58] Although the evidence for ADC as a response biomarker in bone marrow is more extensive, early changes in fat fraction have been shown to predict response and it seems likely that ADC and fat fraction will be complimentary metrics.[58]

T2W imaging

Technical background

T2W images are usually acquired using single-shot FSE/TSE (ss-FSE/ss-TSE) sequences. ss-FSE/ss-TSE sequences acquire all of the data required to reconstruct one image in a single echo train[59]. ss-FSE/ss-TSE images exhibit more blurring than conventional FSE/TSE images due to the long echo trains, but their rapid acquisition makes ss-FSE/ss-TSE suitable for WB applications. ss-FSE/ss-TSE images are relatively robust to motion and acceptable images may be obtained using free-breathing acquisitions even in abdominal and thoracic stations.

Clinical applications

T2W images are particularly helpful for imaging malignancies such as breast and prostate cancer where soft tissue and bone disease co-exist. Furthermore, T2W images provide additional information in the case of

Please cite this article as: Winfield JM et al., Whole-body MRI: a practical guide for imaging patients with malignant bone disease, Clinical Radiology, https://doi.org/10.1016/j.crad.2021.04.001

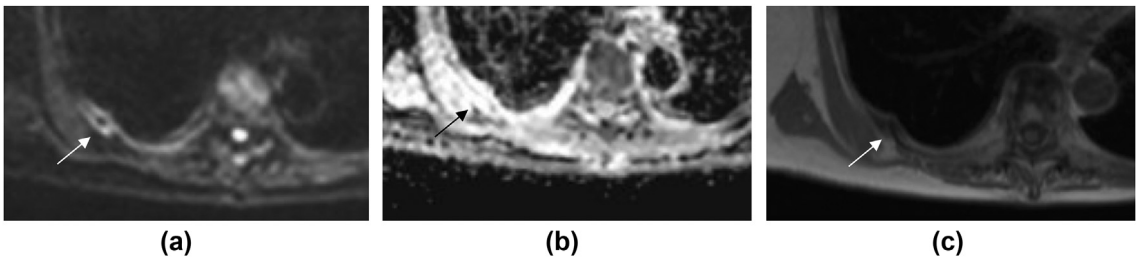

Figure 6 Rib fracture. (a) Axial b = 900 s/mm^2 DW-MRI shows abnormal signal relating to a right sided rib (arrow) and (b) the ADC map shows high ADC indicating oedema (arrow). (c) The corresponding fat-only Dixon MRI image demonstrates an underlying well-marginated likely benign fracture (arrow).

malignant spinal cord compression or local relapse in the prostate. Although visceral and nodal metastases are often detected on DW-MRI, the T2W sequences add diagnostic confidence and can also be reviewed for incidental findings. Although incidental findings are common, they are usually characterised by WB-MRI and only a small number (3%) of additional investigations are triggered.[48]

Structured clinical reporting

The proposed WB-MRI protocols provide the breadth of detail necessary to inform and support clinical decision-making.[17,18] In our experience, structured reporting templates serve to ensure that the reporting radiologist follows a systematic review process, facilitates interpretation by the clinician with signposting of significant findings, and improves opportunities for targeted data extraction for research and audit. An example of structured clinical reporting of a WB-MRI of a patient with myeloma (Fig 1) is provided below in Box 1.

Informatics developments and future vision

A key consideration when performing WB-MRI is the large volume of data that is acquired for each examination. Typical patient studies currently require around 1 GB of storage due to (i) the large FOVs required resulting in the acquisition of 200–300 axial slices, and (ii) the acquisition of multiple image contrasts including DW-MRI, Dixon, and T2W WB images, plus additional series such as sagittal

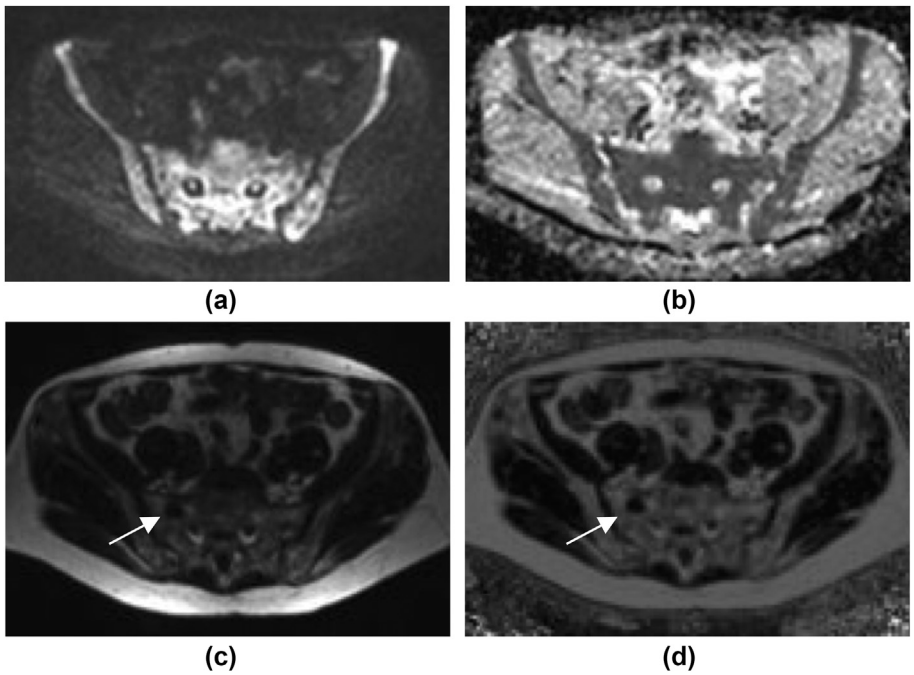

Figure 7 Diffuse marrow hypercellularity obscures focal lesions on DW-MRI. (a) Axial b = 900 s/mm^2 DW-MRI shows diffuse abnormal high signal in the bone marrow and (b) impeded diffusion on the ADC map, which suggests diffuse hypercellularity. (c) Corresponding fat only and (d) FF map from Dixon MRI shows a focal lesion in the right side of the sacrum (arrows), which is not discernible on DW-MRI.

Please cite this article as: Winfield JM et al., Whole-body MRI: a practical guide for imaging patients with malignant bone disease, Clinical Radiology, https://doi.org/10.1016/j.crad.2021.04.001

Box 1
Structured clinical reporting of a whole-body magnetic resonance imaging of a patient with myeloma.

Clinical indication:	? New diagnosis of myeloma
Findings:	WB-MRI has been performed from the skull vertex to the knees and only the proximal humeri are included in the field of view. The protocol has been supplemented with axial T2W images through T1–T6
Spine:	Vertebral body heights are maintained. There is paramedullary disease encroaching the spinal canal at T2–T5 effacing cerebrospinal fluid (CSF) with cord compression
Marrow:	There is a large burden of multifocal disease throughout the skeleton with the majority of lesions measuring >1 cm. This includes multifocal disease in the femora; however, on MRI there is no evidence of cortical breach
Posterior iliac crests:	Appearances suggest that posterior iliac crest trephining will sample representative marrow
Extramedullary disease:	None
Incidental findings	None concerning
Opinion:	There is a heavy burden of widespread multifocal disease in the bone marrow with cord compression from T2–5. This includes disease in weight-bearing bones, and particularly if there are local symptoms, targeted plain films are recommended to assess for cortical oss

spine images. It is, therefore, essential that robust informatics pipelines be developed in order to assist radiologists with the interpretation of these data and maximise the accuracy of clinical findings.

Delineation of disease in WB-MRI datasets is of paramount importance if the methodology is to be successful as a quantitative technique for assessing patient response to therapy and predicting patient outcome. Numerous studies have demonstrated the potential of average or median ADC values derived from disease (Fig 8) as an imaging biomarker for response and patient prognosis in myeloma,[35] and metastatic prostate[34,46,60] and breast cancers[61,62]; however,

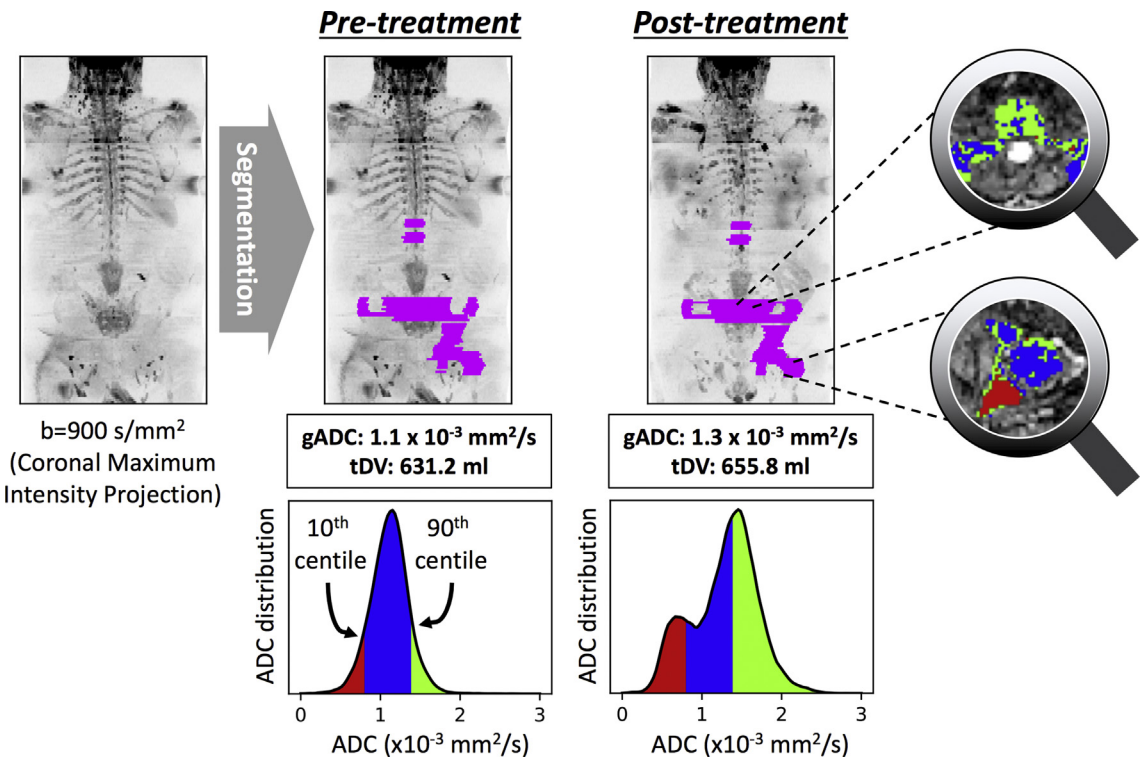

Figure 8 Automatic and semi-automatic segmentation methods of bony disease (purple) in WB-MRI enable extraction of two quantitative biomarkers of response: the global average ADC (gADC) and total disease volume (tDV). By assessing changes in these parameters after treatment, it may be possible to identify patients who are benefitting from treatment at an early stage and thus guide personalised therapy; however, investigation of the distribution of ADC values also reveals significant heterogeneity of response, which can be investigate to further elucidate patterns of response in patients. In this case of a patient with metastatic prostate disease, we obtain the 10th and 90th percentile of the pre-treatment ADC distribution, and apply these thresholds to the post-treatment distribution to highlight regions of ADC decrease (red), ADC increase (green), and no change (blue) after therapy. Such statistical approaches may be used to highlight differential patterns of response on the ADC maps (right).

Please cite this article as: Winfield JM et al., Whole-body MRI: a practical guide for imaging patients with malignant bone disease, Clinical Radiology, https://doi.org/10.1016/j.crad.2021.04.001

manual delineation of disease in these large datasets is not practical in the clinic and methods for automatic[63] or even semi-automatic[60] contouring are an active area of research.

Recent evidence demonstrates that response in WB disease can be highly heterogeneous, with patterns of both intra- and inter-tumour response heterogeneity occurring within individual patients.[64] Non-invasive imaging provides a unique opportunity to probe and characterise heterogeneous response to systemic treatments, without the requirement for multiple or serial biopsies (Fig 8). Computational approaches that can discriminate and highlight responding from non-responding disease in each patient will provide a window of opportunity to switch or augment treatment at an early stage and improve patient outcome.

The complexity of clinical reporting from WB-MRI is well known and has driven the radiological community to provide guidelines for reporting finding in multiple myeloma,[17] and metastatic prostate cancer.[18] Development of electronic, structured reporting systems will help support the adoption of these guidelines, and combining structured reports with adequate data repositories and data-mining tools could facilitate investigative studies of other imaging biomarkers.

Informatics developments have also led to the generation of novel image contrast in WB-MRI. Computed DW-MRI (cDWI) is an approach whereby images are obtained in post-processing with different b-values to those acquired at the scanner, potentially improving visualisation of disease for certain tumour types.[65–67] This methodology has now been adopted on many clinical scanners.

There is no doubt that artificial intelligence and machine learning (AI/ML) will have considerable impact on the future analysis of WB-MRI. AI/ML has dramatically accelerated the development of powerful processing tools throughout medical imaging fields, including algorithms for region delineation,[68–70] image denoising,[71] image reconstruction,[72,73] tissue characterisation,[74] and artefact removal.[75] Many of these issues are still to be addressed in WB-MRI, but it should be noted that these algorithms are data-hungry and reliant on the curation of large representative datasets acquired at multiple institutions; AI/ML models should ideally be trained/tested using images acquired from different vendors and at different field-strengths. In the UK, NHSX and NICE have recently published guidelines and evidence standards to support the safe adoption of new digital health technologies (including AI/ML) within the NHS.[76,77]

Conclusion

WB-MRI is now a crucial tool for delivering precision therapy for patients with myeloma at diagnosis and relapse and metastatic bone disease, in particular in the response assessment setting. For patients with high-risk myeloma or oligo/non-secretory myeloma WB-MRI can be used as a non-invasive surveillance tool and response assessment is particularly helpful for patients who have undergone multiple lines of therapy when clonal disease evolution is more likely to result in heterogeneous response. Mature acquisition protocols are now enabling much wider adoption and new insights on bone disease are stimulating novel therapeutic opportunities. The non-invasive nature of WB-MRI is also attracting increasing interest for paediatric applications. Current development strategies are focusing on reducing acquisition times, automating disease measurements and detection of pulmonary nodules, which is a limitation of MRI. WB-MRI is possible on modern MRI scanners from all main manufacturers, and clinical adoption will be improved with increased resources and training.

Conflict of interest

The authors declare no conflict of interest.

Acknowledgements

We acknowledge funding from Cancer Research UK and Engineering and Physical Sciences Research Council support to the Cancer Imaging Centre at the Institute of Cancer Research and Royal Marsden Hospital in association with the Medical Research Council and Department of Health C1060/A10334, C1060/A16464 and National Health Service funding to the National Institute for Health Research Biomedical Research Centre, Experimental Cancer Medicine Centre, the Clinical Research Facility in Imaging, and the Cancer Research Network. The views expressed in this publication are those of the author(s) and not necessarily those of the National Health Service, the National Institute for Health Research or the Department of Health.

References

1. Cancer Research UK. Cancer statistics for the UK. Available at: https://www.cancerresearchuk.org/health-professional/cancer-statistics-for-the-uk. [Accessed 21 June 2020].
2. Eisenhauer EA, Therasse P, Bogaerts J, *et al*. New response evaluation criteria in solid tumours: revised RECIST guideline (version 1.1). *Eur J Canc* 2009;**45**:228–47. https://doi.org/10.1016/j.ejca.2008.10.026.
3. Scher HI, Morris MJ, Stadler WM, *et al*. Trial design and objectives for castration-resistant prostate cancer: updated recommendations from the Prostate Cancer Clinical Trials Working Group 3. *J Clin Oncol* 2016;**34**:1402.
4. Morone M, Bali MA, Tunariu N, *et al*. Whole-body MRI: current applications in oncology. *AJR Am J Roentgenol* 2017;**209**:W336–49. https://doi.org/10.2214/AJR.17.17984.
5. Pawlyn C, Fowkes L, Otero S, *et al*. Whole-body diffusion-weighted MRI: a new gold standard for assessing disease burden in patients with multiple myeloma? *Leukemia* 2016;**30**:1446–8. https://doi.org/10.1038/leu.2015.338.
6. Rasche L, Angtuaco E, McDonald JE, *et al*. Low expression of hexokinase-2 is associated with false-negative FDG–positron emission tomography in multiple myeloma. *Blood* 2017;**130**:30–4.
7. Sachpekidis C, Mosebach J, Freitag MT, *et al*. Application of ^{18}F-FDG PET and diffusion weighted imaging (DWI) in multiple myeloma: comparison of functional imaging modalities. *Am J Nucl Med Mol Imag* 2015;**5**:479.
8. Miles A, Evans RE, Halligan S, *et al*. Predictors of patient preference for either whole body magnetic resonance imaging (WB-MRI) or CT/PET-CT for staging colorectal or lung cancer. *J Med Imaging Radiat Oncol* 2020;**64**:537–45. https://doi.org/10.1111/1754-9485.13038.
9. Gillessen S, Attard G, Beer TM, *et al*. Management of patients with advanced prostate cancer: report of the Advanced Prostate Cancer

Consensus Conference 2019. *Eur Urol* 2020;**77**:508–47. https://doi.org/10.1016/j.eururo.2020.01.012.
10. Perez-Lopez R, Tunariu N, Padhani AR, *et al*. Imaging diagnosis and follow-up of advanced prostate cancer: clinical perspectives and state of the art. *Radiology* 2019;**292**:273–86. https://doi.org/10.1148/radiol.2019181931.
11. Trabulsi EJ, Rumble RB, Jadvar H, *et al*. Optimum imaging strategies for advanced prostate cancer: ASCO guideline. *J Clin Oncol* 2020;**19**:02757.
12. Sundahl N, Gillessen S, Sweeney C, *et al*. When what you see is not always what you get: raising the bar of evidence for new diagnostic imaging modalities. *Eur Urol* 2021;**79**:565–7. https://doi.org/10.1016/j.eururo.2020.07.029.
13. Rajkumar SV, Dimopoulos MA, Palumbo A, *et al*. International Myeloma Working Group updated criteria for the diagnosis of multiple myeloma. *Lancet Oncol* 2014;**15**:538–48. https://doi.org/10.1016/S1470-2045(14)70442-5.
14. Messiou C, Kaiser M. Whole-body imaging in multiple myeloma. *Magn Reson Imag Clin N Am* 2018;**26**:509–25. https://doi.org/10.1016/j.mric.2018.06.006.
15. National Institute for Health and Care Excellence (NICE). Myeloma: diagnosis and management (NG35). Available at: www.nice.org.uk/guidance/ng35 (accessed: 27th June 2020).
16. Kaiser MF, Boyd K, Koh DM, *et al*. Improving real-world myeloma patient access to whole body MRI through "open-access" knowledge sharing: the UK experience. *eJHaem* 2020;**1**:361–3. https://doi.org/10.1002/jha2.25.
17. Messiou C, Hillengass J, Delorme S, *et al*. Guidelines for acquisition, interpretation, and reporting of whole-body MRI in myeloma: myeloma response assessment and diagnosis system (MY-RADS). *Radiology* 2019;**291**:5–13. https://doi.org/10.1148/radiol.2019181949.
18. Padhani AR, Lecouvet FE, Tunariu N, *et al*. METastasis Reporting and Data System for Prostate Cancer: practical guidelines for acquisition, interpretation, and reporting of whole-body magnetic resonance imaging-based evaluations of multiorgan involvement in advanced prostate cancer. *Eur Urol* 2017;**71**:81–92. https://doi.org/10.1016/j.eururo.2016.05.033.
19. Westerland OA, Pratt G, Kazmi M, *et al*. National survey of imaging practice for suspected or confirmed plasma cell malignancies. *Br J Radiol* 2019;**91**:20180462.
20. Royal College of Radiologists. Magnetic resonance imaging (MRI) equipment, operations and planning in the NHS. Available at: https://www.rcr.ac.uk/sites/default/files/cib_mri_equipment_report.pdf (accessed: 27th June 2020).
21. Barnes A, Alonzi R, Blackledge M, *et al*. UK quantitative WB-DWI technical workgroup: consensus meeting recommendations on optimisation, quality control, processing and analysis of quantitative whole-body diffusion-weighted imaging for cancer. *Br J Radiol* 2018;**91**:20170577. https://doi.org/10.1259/bjr.20170577.
22. Hennig J, Nauerth A, Friedburg H. RARE imaging: a fast imaging method for clinical MR. *Magn Reson Med* 1986;**3**:823–33. https://doi.org/10.1002/mrm.1910030602.
23. Bydder G, Young I. MR imaging: clinical use of the inversion recovery sequence. *J Comput Assist Tomogr* 1985;**9**:659–75.
24. Sung JK, Jee W-H, Jung J-Y, *et al*. Differentiation of acute osteoporotic and malignant compression fractures of the spine: use of additive qualitative and quantitative axial diffusion-weighted MR imaging to conventional MR imaging at 3.0 T. *Radiology* 2014;**271**:488–98.
25. Einstein A. On the motion of small particles suspended in liquids at rest required by the molecular-kinetic theory of heat. *Ann Phys* 1905;**17**:208.
26. Norris DG. The effects of microscopic tissue parameters on the diffusion weighted magnetic resonance imaging experiment. *NMR Biomed* 2001;**14**:77–93. https://doi.org/10.1002/nbm.682.
27. Taouli B, Beer AJ, Chenevert T, *et al*. Diffusion-weighted imaging outside the brain: consensus statement from an ISMRM-sponsored workshop. *J Magn Reson Imag* 2016;**44**:521–40. https://doi.org/10.1002/jmri.25196.
28. Mansfield P. Multi-planar image formation using NMR spin echoes. *J Phys C: Solid State Phys* 1977;**10**:L55. https://doi.org/10.1088/0022-3719/10/3/004.
29. Stehling MK, Turner R, Mansfield P. Echo-planar imaging: magnetic resonance imaging in a fraction of a second. *Science* 1991;**254**:43–50. https://doi.org/10.1126/science.1925560.
30. Stejskal EO, Tanner JE. Spin diffusion measurements: spin echoes in the presence of a time-dependent field gradient. *J Chem Phys* 1965;**42**:288–92.
31. Le Bihan D, Breton E, Lallemand D, *et al*. Separation of diffusion and perfusion in intravoxel incoherent motion MR imaging. *Radiology* 1988;**168**:497–505.
32. Winfield JM, Collins DJ, Priest AN, *et al*. A framework for optimization of diffusion-weighted MRI protocols for large field-of-view abdominal-pelvic imaging in multicenter studies. *Med Phys* 2016;**43**:95. https://doi.org/10.1118/1.4937789.
33. Malyarenko DI, Newitt D, JW L, *et al*. Demonstration of nonlinearity bias in the measurement of the apparent diffusion coefficient in multicenter trials. *Magn Reson Med* 2016;**75**:1312–23. https://doi.org/10.1002/mrm.25754.
34. Perez-Lopez R, Lorente D, Blackledge MD, *et al*. Volume of bone metastasis assessed with whole-body diffusion-weighted imaging is associated with overall survival in metastatic castration-resistant prostate cancer. *Radiology* 2016;**280**:151–60.
35. Giles SL, Messiou C, Collins DJ, *et al*. Whole-body diffusion-weighted MR imaging for assessment of treatment response in myeloma. *Radiology* 2014;**271**:785–94. https://doi.org/10.1148/radiol.13131529.
36. Padhani AR, van Ree K, Collins DJ, *et al*. Assessing the relation between bone marrow signal intensity and apparent diffusion coefficient in diffusion-weighted MRI. *AJR Am J Roentgenol* 2013;**200**:163–70.
37. Saya S, Killick E, Thomas S, *et al*. Baseline results from the UK SIGNIFY study: a whole-body MRI screening study in TP53 mutation carriers and matched controls. *Fam Canc* 2017;**16**:433–40. https://doi.org/10.1007/s10689-017-9965-1.
38. Dietrich O, Heiland S, Sartor K. Noise correction for the exact determination of apparent diffusion coefficients at low SNR. *Magn Reson Med* 2001;**45**:448–53.
39. Winfield JM, Douglas NH, deSouza NM, *et al*. Phantom for assessment of fat suppression in large field-of-view diffusion-weighted magnetic resonance imaging. *Phys Med Biol* 2014;**59**:2235–48. https://doi.org/10.1088/0031-9155/59/9/2235.
40. Mürtz P, Krautmacher C, Träber F, *et al*. Diffusion-weighted whole-body MR imaging with background body signal suppression: a feasibility study at 3.0 Tesla. *Eur Radiol* 2007;**17**:3031–7.
41. Maehara M, Ikeda K, Kurokawa H, *et al*. Diffusion-weighted echo-planar imaging of the head and neck using 3-T MRI: investigation into the usefulness of liquid perfluorocarbon pads and choice of optimal fat suppression method. *Magn Reson Imag* 2014;**32**:440–5.
42. Pearce T, Philip S, Brown J, *et al*. Bone metastases from prostate, breast and multiple myeloma: differences in lesion conspicuity at short-tau inversion recovery and diffusion-weighted MRI. *Br J Radiol* 2012;**85**:1102–6.
43. Padhani AR, Liu G, Mu-Koh D, *et al*. Diffusion-weighted magnetic resonance imaging as a cancer biomarker: consensus and recommendations. *Neoplasia* 2009;**11**:102–25.
44. Palma DA, Olson R, Harrow S, *et al*. Stereotactic ablative radiotherapy versus standard of care palliative treatment in patients with oligometastatic cancers (SABR-COMET): a randomised, phase 2, open-label trial. *Lancet* 2019;**393**:2051–8.
45. Messiou C, Giles S, Collins DJ, *et al*. Assessing response of myeloma bone disease with diffusion-weighted MRI. *Br J Radiol* 2012;**e85**:1198–203. https://doi.org/10.1259/bjr/52759767.
46. Perez-Lopez R, Mateo J, Mossop H, *et al*. Diffusion-weighted imaging as a treatment response biomarker for evaluating bone metastases in prostate cancer: a pilot study. *Radiology* 2017;**283**:168–77.
47. Lavdas I, Rockall AG, Castelli F, *et al*. Apparent diffusion coefficient of normal abdominal organs and bone marrow from whole-body DWI at 1.5 T: the effect of sex and age. *AJR Am J Roentgenol* 2015;**205**:242–50.
48. Wale A, Pawlyn C, Kaiser M, *et al*. Frequency, distribution and clinical management of incidental findings and extramedullary plasmacytomas in whole body diffusion weighted magnetic resonance imaging in patients with multiple myeloma. *Haematologica* 2016;**101**:142–4. https://doi.org/10.3324/haematol.2015.139816.
49. Ahmed N, Sriskandarajah P, Burd C, *et al*. Detection of avascular necrosis on routine diffusion-weighted whole body MRI in patients with multiple myeloma. *Br J Radiol* 2019;**92**:20180822.

Please cite this article as: Winfield JM et al., Whole-body MRI: a practical guide for imaging patients with malignant bone disease, Clinical Radiology, https://doi.org/10.1016/j.crad.2021.04.001

50. Dixon WT. Simple proton spectroscopic imaging. *Radiology* 1984;**153**:189–94. https://doi.org/10.1148/radiology.153.1.6089263.
51. Kukuk GM, Hittatiya K, Sprinkart AM, *et al*. Comparison between modified Dixon MRI techniques, MR spectroscopic relaxometry, and different histologic quantification methods in the assessment of hepatic steatosis. *Eur Radiol* 2015;**25**:2869–79.
52. Bydder M, Yokoo T, Hamilton G, *et al*. Relaxation effects in the quantification of fat using gradient echo imaging. *Magn Reson Imag* 2008;**26**:347–59.
53. Liu CY, McKenzie CA, Yu H, *et al*. Fat quantification with IDEAL gradient echo imaging: correction of bias from T1 and noise. *Magn Reson Med* 2007;**58**:354–64.
54. Reeder SB, Hu HH, Sirlin CB. Proton density fat-fraction: a standardized MR-based biomarker of tissue fat concentration. *J Magn Reson Imag* 2012;**36**:1011–4. https://doi.org/10.1002/jmri.23741.
55. Hardy PA, Hinks RS, Tkach JA. Separation of fat and water in fast spin-echo MR imaging with the three-point Dixon technique. *J Magn Reson Imag* 1995;**5**:181–5. https://doi.org/10.1002/jmri.1880050213.
56. Maeder Y, Dunet V, Richard R, *et al*. Bone marrow metastases: T2-weighted Dixon spin-echo fat images can replace T1-weighted spin-echo images. *Radiology* 2018;**286**:853–64. https://doi.org/10.1148/radiol.2017170325.
57. Sasiponganan C, Yan K, Pezeshk P, *et al*. Advanced MR imaging of bone marrow: quantification of signal alterations on T1-weighted Dixon and T2-weighted Dixon sequences in red marrow, yellow marrow, and pathologic marrow lesions. *Skeletal Radiol* 2020;**49**:541–8. https://doi.org/10.1007/s00256-019-03303-z.
58. Latifoltojar A, Hall-Craggs M, Rabin N, *et al*. Whole body magnetic resonance imaging in newly diagnosed multiple myeloma: early changes in lesional signal fat fraction predict disease response. *Br J Haematol* 2017;**176**:222–33. https://doi.org/10.1111/bjh.14401.
59. Semelka RC, Kelekis NL, Thomasson D, *et al*. HASTE MR imaging: description of technique and preliminary results in the abdomen. *J Magn Reson Imag* 1996;**6**:698–9. https://doi.org/10.1002/jmri.1880060420.
60. Blackledge MD, Collins DJ, Tunariu N, *et al*. Assessment of treatment response by total tumor volume and global apparent diffusion coefficient using diffusion-weighted MRI in patients with metastatic bone disease: a feasibility study. *PloS One* 2014;**9**:e91779.
61. Padhani AR, Makris A, Gall P, *et al*. Therapy monitoring of skeletal metastases with whole-body diffusion MRI. *J Magn Reson Imag* 2014;**39**:1049–78. https://doi.org/10.1002/jmri.24548.
62. Zugni F, Ruju F, Pricolo P, *et al*. The added value of whole-body magnetic resonance imaging in the management of patients with advanced breast cancer. *PloS One* 2018;**13**:e0205251, https://doi.org/10.1371/journal.pone.0205251.
63. Lavdas I, Glocker B, Kamnitsas K, *et al*. Fully automatic, multiorgan segmentation in normal whole body magnetic resonance imaging (MRI), using classification forests (CFs), convolutional neural networks (CNNs), and a multi-atlas (MA) approach. *Med Phys* 2017;**44**:5210–20.
64. Blackledge MD, Rata M, Tunariu N, *et al*. Visualizing whole-body treatment response heterogeneity using multi-parametric magnetic resonance imaging. *J Algorith Comput Technol* 2016;**10**:290–301.
65. Blackledge MD, Leach MO, Collins DJ, *et al*. Computed diffusion-weighted MR imaging may improve tumor detection. *Radiology* 2011;**261**:573–81. https://doi.org/10.1148/radiol.11101919.
66. Cheng L, Blackledge MD, Collins DJ, *et al*. T2-adjusted computed diffusion-weighted imaging: a novel method to enhance tumour visualisation. *Comput Biol Med* 2016;**79**:92–8. https://doi.org/10.1016/j.compbiomed.2016.09.022.
67. O'Flynn EA, Blackledge M, Collins D, *et al*. Evaluating the diagnostic sensitivity of computed diffusion-weighted MR imaging in the detection of breast cancer. *J Magn Reson Imag* 2016;**44**:130–7. https://doi.org/10.1002/jmri.25131.
68. Havaei M, Davy A, Warde-Farley D, *et al*. Brain tumor segmentation with deep neural networks. *Med Image Anal* 2017;**35**:18–31. https://doi.org/10.1016/j.media.2016.05.004.
69. Kamnitsas K, Ferrante E, Parisot S, *et al*. DeepMedic for brain tumor segmentation. In: Crimi A, Menze B, Maier O, *et al*., editors. *Brainlesion: glioma, multiple sclerosis, stroke and traumatic brain injuries. BrainLes 2016. Lecture notes in computer science* **10154**. Cham: Springer; 2016, https://doi.org/10.1007/978-3-319-55524-9_14.
70. Ronneberger O, Fischer P, Brox T. U-net: convolutional networks for biomedical image segmentation. In: *International Conference on Medical image computing and computer-assisted intervention*. Cham: Springer; 2015. p. 234–41.
71. Tian C, Fei L, Zheng W, *et al*. *Deep learning on image denoising: an overview*. arXiv; 2019. arXiv:191213171.
72. Hyun CM, Kim HP, Lee SM, *et al*. Deep learning for undersampled MRI reconstruction. *Phys Med Biol* 2018;**63**:135007. https://doi.org/10.1088/1361-6560/aac71a.
73. Zhu B, Liu JZ, Cauley SF, *et al*. Image reconstruction by domain-transform manifold learning. *Nature* 2018;**555**:487–92. https://doi.org/10.1038/nature25988.
74. Blackledge MD, Winfield JM, Miah A, *et al*. Supervised machine-learning enables segmentation and evaluation of heterogeneous post-treatment changes in multi-parametric MRI of soft-tissue sarcoma. *Front Oncol* 2019;**9**:941. https://doi.org/10.3389/fonc.2019.00941.
75. Xie S, Zheng X, Chen Y, *et al*. Artifact removal using improved GoogLeNet for sparse-view CT reconstruction. *Sci Rep* 2018;**8**:1–9.
76. National Institute for Health and Care Excellence (NICE). *Evidence standards framework for digital health technologies*. 2019. Available at: https://www.nice.org.uk/about/what-we-do/our-programmes/evidence-standards-framework-for-digital-health-technologies (accessed: 27th June 2020).
77. Department of Health and Social Care. *Code of conduct for data-driven health and care technology*. 2019. Available at: https://www.gov.uk/government/publications/code-of-conduct-for-data-driven-health-and-care-technology/initial-code-of-conduct-for-data-driven-health-and-care-technology (accessed: 27th June 2020).

Please cite this article as: Winfield JM et al., Whole-body MRI: a practical guide for imaging patients with malignant bone disease, Clinical Radiology, https://doi.org/10.1016/j.crad.2021.04.001